A dynamically based method for estimating the Atlantic overturning circulation at 26°N from satellite altimetry

Alejandra Sanchez-Franks[1], Eleanor Frajka-Williams[1], Ben I. Moat[1], and David A. Smeed[1]

[1]National Oceanography Centre, University of Southampton Waterfront Campus, European Way, Southampton, SO14 3ZH, UK.

Correspondence: Alejandra Sanchez-Franks (alsf@noc.ac.uk)

Abstract. The large-scale system of ocean currents that transport warm surface (1000 m) waters northward and return cooler waters southward is known as the Atlantic meridional overturning circulation (AMOC). Variations in the AMOC have significant repercussions for the climate system, hence there is a need for long term monitoring of AMOC fluctuations. Currently the longest record of continuous directly measured AMOC changes is from the RAPID-MOCHA-WBTS programme, initi-

5 ated in 2004. The RAPID programme, and other mooring programmes, have revolutionised our understanding of large-scale circulation, however, by design they are constrained to measurements at a single latitude.

High global coverage of surface ocean data from satellite altimetry is available since the launch of TOPEX/Poseidon satellite in 1992 and has been shown to provide reliable estimates of surface ocean transports on interannual time scales. Here we show that a direct calculation of ocean circulation from satellite altimetry compares well with transport estimates from the

10 26°N RAPID array on low frequency (18-month) time scales for the upper mid-ocean transport (UMO; r = 0.75), the Gulf Stream transport through the Florida Straits (r = 0.70), and the AMOC (r = 0.83). The vertical structure of the circulation is also investigated, and it is found that the first baroclinic mode accounts for 83% of the interior geostrophic variability, while remaining variability is explained by the barotropic mode. Finally, the UMO and the AMOC are estimated from historical altimetry data (1993 to 2018) using a dynamically based method that incorporates the vertical structure of the flow. The effective

15 implementation of satellite-based method for monitoring the AMOC at 26°N lays down the starting point for monitoring large-scale circulation at all latitudes.

1   Introduction

The Atlantic meridional overturning circulation (AMOC) is the large-scale oceanic circulation comprised of currents that carry warm, shallow water northward and return cold deep water southward. Variations in the AMOC's strength have significant

20 impact on the Earth's climate system (Srokosz et al., 2012) as the AMOC's northward transport of warm surface waters release heat on the order of 1 PW over the North Atlantic (Trenberth and Caron, 2001), key in maintaining the relatively mild winter climate of northwest Europe (Hall and Bryden, 1982; Pohlmann et al., 2006). On decadal time scale, the AMOC is identified as the underlying driver of latitudinal shifts in the Gulf Stream path (Sanchez-Franks and Zhang, 2015), and changes in the AMOC are a key driver of the Atlantic Multidecadal Variability and associated climate variability (Zhang et al., 2019). On

25 longer time scales, coupled climate models predict significant weakening of the AMOC which results in a reduced northward heat transport associated with increased greenhouse gas forcing (Caesar et al., 2018).

One of the existing programmes monitoring the AMOC is the RAPID-MOCHA-WBTS (RAPID – Meridional Overturning Circulation and Heatflux Array – Western Boundary Time Series; hereafter RAPID) 26°N mooring array, which has been measuring the meridional volume ($\mathrm{m^3s^{-1}}$) transport at 26°N since 2004 (Rayner et al., 2011; Smeed et al., 2014; McCarthy
30 et al., 2015; Moat et al., 2020a,b). The RAPID programme is an international campaign that uses an array of moored instruments at strategic locations in order to continuously estimate AMOC fluctuations (further details in McCarthy et al. (2015)). Key to the RAPID strategy is that the interior of the ocean is largely in geostrophic balance; placing moorings in the western and eastern endpoints of the Atlantic basin, as well as the mid-Atlantic ridge, allows for fluctuations in the vertical density profiles to be simultaneously measured at the mooring locations. By taking the difference between the endpoint measurements, the
35 interior geostrophic flow going through them can be estimated. The density field estimated from the RAPID moorings is affected by long Rossby waves that start off as westward-traveling perturbations (Johnson and Marshall, 2002; Hirschi et al., 2007), altering the east-west density gradient driving AMOC variability.

Mooring array programmes such as RAPID have made step-change advancements in our understanding of the AMOC over the last 15 years (Frajka-Williams et al., 2019), however they are limited to a single line of latitude and alone cannot be
40 used to infer upstream/downstream changes in the larger scale structure of the AMOC. Satellite data provide high spatial coverage of the global oceans. Altimetric measurements collect data of the surface topography of the ocean (i.e. sea surface height; SSH), which is an effective means of measuring large-scale surface circulation and associated dynamics. In particular, westward propagating Rossby waves, or surface intensified flow which is largely of baroclinic structure, are captured by satellite observations (Chelton et al., 2007). Previous efforts to use Earth-observing methods have shown capacity in estimating the
45 large-scale ocean circulation. For example, satellite sea level anomaly (SLA) has been used as a proxy for AMOC transports along 40-50°N (Bingham and Hughes, 2009), and SLA has been linked to east-west pressure along 26°N (Hirschi et al., 2007). Frajka-Williams (2015) found that the relationship between satellite SLA and RAPID dynamic height was robust enough to be used to create a proxy for the AMOC transport. The relationship between dynamic height from RAPID moorings and satellite SSH at 26°N was also found to be robust (Kanzow et al., 2009), however this relationship was found to deteriorate in proximity
50 to the western boundary (Bryden et al., 2009; Clément et al., 2014).

One of the limitations of satellite altimetry is that it only provides information about the sea surface. While this is enough to infer AMOC variability (due to the baroclinic nature of the surface intensified ocean), satellite altimetry cannot tell us anything about the vertical shape of the horizontal velocity which forms part of the AMOC structure. To get around this, previous studies have combined satellite altimetry data with vertical structure of the flow derived from in situ datasets with some success (e.g.
55 Hirschi et al., 2007, 2009; Kanzow et al., 2009; Szuts et al., 2012). Here, we build on these methods using geostrophic principles to develop a satellite-based geostrophic transport; we examine the extent of the contribution of vertical structure of the flow to the total AMOC variability; and quantify the extent at which satellite altimetry can successfully reproduce the meridional overturning circulation.

In the following section (2), a brief overview of data and methods used here are presented. Then an evaluation of the satellite
data and parameters from the RAPID moorings follows in section 3. Rossby wave theory and an in-depth analysis of horizontal
velocity normal modes from RAPID mooring data is shown in section 4. Sections 5 and 6 investigate construction of the upper
mid-ocean, the Gulf Stream, and the AMOC transports from satellite altimetry. Finally, summary and conclusions are given in
section 7.

2 Data and Methods

2.1 Satellite and mooring data

For this study, SLA from the Copernicus Marine Environment Monitoring Service (CMEMS: http://marine.copernicus.eu;
product ID: SEALEVEL_GLO_PHY_L4_REP_OBSERVATIONS_008_047) gridded multimission satellite altimetry is used
to create a proxy for AMOC transport. The CMEMS gridded altimetry includes data from the following satellite missions:
Envisat, Geosat Follow On, Jason-1, TOPEX/Poseidon Interleaved. The satellite product has a $\frac{1}{4}°$ resolution in space and
monthly in time, though the resolution is limited by the underlying track spacing between altimeter passes.

The SLA is compared to data from the RAPID 26°N mooring array. The RAPID array is designed to measure the AMOC
at 26°N by using strategically placed moorings at 3 key regions (Rayner et al., 2011; McCarthy et al., 2015). The first is in
the western boundary, the second at the mid-Atlantic Ridge, and the third along the eastern boundary. The RAPID moorings
provide continuous dynamic height profiles from conductivity, temperature and depth using MicroCAT CTDs. The western
boundary used in the RAPID AMOC calculation includes moorings WB2, WBH2 and WB3 (hereafter referred to as West).
When comparing with the SLA, data from the RAPID moorings WB2 (26.5°N and 76.75°W), WB3 (26.5°N and 76.5°W)
and West are used for the western component, and an amalgamation of data from the eastern boundary moorings between
13.75°W-24.22°W and 23.7-27.9°N (hereafter referred to collectively as EB) are used for the eastern component (section 3
and 4) (Fig. 1a). Further details on the instrumentation and observational strategy of the RAPID mooring array can be found in
McCarthy et al. (2015).

RAPID MicroCATs record on an hourly basis. These data are then postprocessed with a 2-day low pass filter to remove
tidal fluctuations. The resulting data is used to compute transport estimates which are gridded at 12-hour resolution. A 10-day
low pass filtered is applied to final transport estimates. RAPID data used here include temperature, salinity, pressure, dynamic
height, as well as estimates of the upper mid-ocean and AMOC transports from 2004 to 2018 (Moat et al., 2020b), which can
be obtained here: http://www.rapid.ac.uk/rapidmoc/.

In this study, 12-hour and daily data are monthly averaged, the annual seasonal climatology is removed and then smoothed
with an 18-month Gaussian filter over the available time periods. Clément et al. (2014) found that Rossby waves and eddies
are important contributors to geostrophic transport on time scales of 3-8 months and Kanzow et al. (2009) found that eddies
do not affect AMOC on low frequency (interannual to decadal) time scales, hence a 18-month filter is deemed appropriate for
removing the influence of eddies. Finally, the mean over 2004 to 2018, which is the overlapping time period between RAPID
and the SLA, is removed from their respective time-series. When computing correlations, the linear trend from 2004-2018 is

removed from the respective time series, and the statistical significance is determined using the effective degrees of freedom calculated as the length of each time series over the integral time scale of decorrelation (Emery and Thomson, 2001).

2.2 RAPID transport estimates and SLA

95 RAPID defines the AMOC transport 26°N as the sum of three components: the Gulf Stream transport (T_{GS}), the Ekman transport (T_{EK}), and the upper mid-ocean transport (T_{UMO}) (McCarthy et al., 2015):

$$T_{MOC}(t) = T_{GS}(t) + T_{EK}(t) + T_{UMO}(t) \tag{1}$$

The first component, T_{GS}, has been measured by submarine telephone cables in the Florida Straits since 1982 (Baringer and Larsen, 2001) (https://www.aoml.noaa.gov/phod/floridacurrent/index.php). The second component, T_{EK}, is derived from 100 zonal wind stress from ERA5 reanalysis products (Hersbach et al., 2020). The third component, T_{UMO}, is the sum of the western boundary wedge transport (T_{WBW}), the hypsometric mass compensation (T_{EXT}), and the internal geostrophic transport (T_{INT}) over the top 1100 m. T_{WBW} is the northward transport measured between the Abaco Island continental shelf and the WB2 mooring. T_{EXT} functions to compensate T_{UMO} so that the net meridional flow is zero, and T_{INT} is the internal geostrophic [southward] transport.

105 Through geostrophic balance, the meridional mass transport is proportional to the integrated pressure difference between the eastern (P_E) and western (P_W) basin endpoints such that:

$$T(t) = \frac{1}{f\rho_0} \int [P_E(z,t) - P_W(z,t)]dz \tag{2}$$

where f is the Coriolis parameter, and ρ_0 is reference density. Pressure is then related to sea level displacement and the vertical profile of density as follows:

110 $$P = \rho_0 g\eta - \int \rho g dz \tag{3}$$

where g is gravitational acceleration and η is satellite SLA.

From satellite altimetry, we can measure the surface geostrophic velocity:

$$v_s = \frac{g}{f}\left[\frac{\partial \eta}{\partial x}\right] \tag{4}$$

Since the surface geostrophic velocity does not give us information about the vertical structure of the horizontal velocity, time-115 varying geostrophic flow is combined with the first pressure mode to obtain T_{UMO} (section 4 and 5). The T_{GS} is estimated using satellite altimetry and linear regression (section 5). The T_{MOC} is constructed by adding the satellite-derived T_{GS} and T_{UMO} with the T_{EK} obtained from ERA5 wind stress as per Eq. (1) (sections 5 and 6). In the following sections, the relationship between satellite and vertical structure of the flow from the moorings is used to develop a new method for estimating AMOC transport.

3 Evaluation of the satellite and mooring data

120

The CMEMS absolute dynamic topography (ADT) is computed as the sum of SLA and mean dynamic topography (MDT). The MDT is a mean estimate of SSH above the geoid over the given reference period 1993 to 2013 (Rio et al., 2018; further details on this data product here: https://www.aviso.altimetry.fr/en/data/products/auxiliary-products/mdt.html). The ADT shows characteristics of the mean state North Atlantic with negative ADT marking the subpolar gyre in the north ($\geq$ 48°N;

125 Fig. 1a) and positive ADT delimiting the subtropical gyre, largely occupying the region between 15°N and 40°N (< 40°N; Fig. 1a). Key features are observed at 36°N, where positive ADT represents the Gulf Stream as it separates from the coast at Cape Hatteras (Fig. 1a) and flows north as a free-wheeling jet, eventually feeding into the North Atlantic Current on its path northward. The negative ADT around the region of the Grand Banks (48°N) is representative of the equatorward flowing Labrador Current that supplies the Slope Sea just north of the Gulf Stream. The Labrador Current is also part of the surface flowing

130 limb of the AMOC. The apparent bipolar structure over the North Atlantic is similar to the EOF mode 1 of the North Atlantic, characterized by Zhang (2008) as the AMOC fingerprint. The standard deviation of the ADT shows most of the variability is contained within the region of the Gulf Stream after it separates from Cape Hatteras (Fig. 1b). This variability is due to the large latitudinal shifts in the Gulf Stream position (Sanchez-Franks et al., 2016).

In the region of RAPID 26.5°N mooring array (Fig. 1a,b), the time-varying ADT at western and eastern points show sub-

135 stantially higher mean and fluctuations in the western boundary (0.73 m rms) compared to the eastern boundary (0.21 m rms) over the 2004 to 2018 period (Fig. 1c). Variability from the cross-basin pressure gradient is largely driven by the variability along the western boundary on lower frequency (periods longer than a year) timescales (Frajka-Williams, 2015).

3.1 Surface variability

The RAPID programme estimates geostrophic transport from the difference between the basinwide eastern and western end-

140 point pressure fluctuations (Eq. 2). Correspondingly, to construct a T_{UMO} estimate from satellite altimetry, the time-varying east-west SLA difference ($\Delta\eta$) is compared at each gridpoint with the RAPID T_{UMO}.

Fig. 2a shows the correlation between RAPID T_{UMO} and $\Delta\eta$ at each gridpoint, where the eastern point remains fixed at the first easternmost SLA gridpoint at each latitude and the western point shifts longitudinally in the westward direction. In general correlations are highest in the western part of the basin in the 26-30°N latitudinal band, and in the east for roughly the

145 same latitudes between 25-35°W (Fig. 2a). It is interesting to note that the correlations along the RAPID line are lower than those found at higher latitudes 27-30°N. This could be due to an improvement in the signal to noise ratio further north.

The correlation map illustrates the optimal choice of longitude and latitude coordinates for max correlation of $\Delta\eta$ with RAPID T_{UMO}, r = 0.74 (statistically significant at 95% level), where the easternmost SLA gridpoint is located at 27.875°N and 13.125°W and the western SLA gridpoint is located at 27.875°N and 74.375°W (Fig. 2a). The east and west dynamic

150 height measurements from the moorings make up the interior geostrophic component of the RAPID T_{UMO} (section 2.2); however, the T_{UMO} also includes contribution from the Antilles Current. For the satellite data to account for as much of the upper mid ocean transport variability as possible, it is advantageous to use satellite endpoints as shown in Fig. 2a to calculate

$\Delta\eta$, which here appears to better reflects the changes in the meridional mass transport. This is consistent with other studies which have similarly found higher agreement between RAPID T_{UMO} transport and satellite variability north of 26.5°N (e.g.
155 Frajka-Williams, 2015).

3.2 Variability in the vertical

In order to determine how well the SLA can estimate the surface (0-1000 m) circulation, it is useful to assess to what depth the variability from SLA captures sub-surface variability. Thus SLA is compared to the dynamic height at every depth from the surface to 1100 dbar from the RAPID moorings in the western and eastern boundary. Dynamic height (ϕ) is calculated from
160 the mooring density profiles as:

$$\phi(p) = \int \delta(p')dp' \qquad (5)$$

Where the specific volume anomaly (δ) is defined as $\delta = \frac{1}{\rho}$. Fig. 2b shows the correlation (r values) between SLA west and east gridpoints (as indicated in previous section) and dynamic height from the RAPID moorings: West, WB3 and EB. Here the respective RAPID mooring dynamic height has been referenced at the surface to SLA to get a correlation value of 1 at
165 the surface which decreases with depth. In the western boundary, SLA at 27.875°N and 74.375°W is compared with both WB3 and West, and the correlation in the top 1100 dbar is found to be everywhere greater than 0.79 (r = 0.79; statistically significant at 95% level). SLA has a higher correlation with dynamic height at mooring West, compared to WB3, maintaining a statistically significant correlation coefficient above r = 0.88 (statistically significant at 95% level) in the top 1100 dbar. Correlation between SLA and WB3 decreases more abruptly at around 300 dbar. In the eastern boundary, correlation between
170 SLA at 27.875°N and 13.125°W and dynamic height at EB is similarly high throughout the top 1100 dbar, albeit weaker compared with the western boundary mooring, with correlations from r = 1 at the surface decreasing to r = 0.77 (statistically significant at 95% level) at 1100 dbar (Fig. 2b). These results suggest that the variability observed at the sea surface is a good measure and coherent with variability to at least 1000 dbar. This is in agreement with Clément et al. (2014) who showed that isopycnal displacements at the RAPID mooring locations agree well with satellite data.

175 ## 4 Rossby wave theory and horizontal velocity modes

4.1 Westward propagation

Wind stress and density fluctuations dominate AMOC variability on seasonal and sub-annual time scales (Hirschi et al., 2007). Wind-driven variability may also play a role on interannual time scales, for example during the winter of 2009/2010, anomalous wind-driven Ekman transport contributed to interannual AMOC fluctuations (Zhao and Johns, 2014; Evans et al., 2017).
180 However, density variability in the upper 1000 m has also been identified as a leading driver of the AMOC on interannual time scales (Hirschi et al., 2007). This density variability is associated with isopycnal perturbations that travel westward as long Rossby waves. The Rossby waves impact the upper mid-ocean component of the AMOC transport through their effect on the east-west density structure of the basin.

The changes in the surface (top 1000 m) density field from westward propagation are visible as a sea surface signal and
185 have been shown to be captured by satellite altimetry. Altimeters are most likely to reflect the first baroclinic mode, and by
association motion of the main thermocline, due to the nature of baroclinic modes which is surface intensified (Wunsch, 1997).
In the subtropical North Atlantic, studies have used satellite altimetry to track westward propagating anomalies (e.g. Hirschi
et al., 2007; Kanzow et al., 2009; Clément et al., 2014). A Hovmoller of SLA along the 26.5°N RAPID line shows how
perturbations in the eastern boundary propagate westwards up to 79°W before they reach the Bahamas and abruptly diminish
190 (Fig. 3). Westward propagation is visible at monthly resolution and even to some extent with 18-month smoothing applied to
the data (Fig. 3b). Amplitudes in the western boundary are larger compared to the eastern boundary, and particularly prominent
during 1996-97, 2003-04, 2006, and post 2015. Interannual variations are observed in the western basin (between 70° and
80°W) and the strong positive anomalies apparent during 2003-2004 and negative anomalies in 2006-2007 are consistent with
Kanzow et al. (2009, their Fig. 5). The speed of these westward propagating anomalies is typically similar to baroclinic Rossby
195 wave phase speed (Gill, 1982; Killworth and Blundell, 2003; Hirschi et al., 2007).

4.2 Modal decomposition

Sea surface signals observed by satellite altimetry reflect changes in the top (1000 m) stratified ocean. Though satellite altimetry
can measure surface geostrophic velocities, it cannot be used to infer the vertical structure of the flow. To understand the
contribution of the flow's vertical structure to the meridional mass transport, and how that impacts satellite-derived transport,
200 pressure modes derived from RAPID mooring data are examined.

The vertical structure of the flow is assessed using normal mode decomposition, assuming a flat bottomed and motionless
ocean (Gill, 1982), using data from the RAPID moorings at the western (West, WB3) and eastern (EB) boundary. The normal
mode decomposition for the given mode number n = 0,1,2. . . is determined from the Sturm-Liouville Eq.:

$$\frac{d^2G_n(z)}{dz^2} + \frac{N^2(z)}{c_e^2}G_n(z) = 0,$$ (6)

205 $$F_n(z) = \frac{dG_n(z)}{dz}$$ (7)

Where $N(z)$ is the Brunt-Vaisala frequency and c_e^2 is the phase/modal speed of the waves. The boundary conditions are defined
as $G_n = 0$ at $z = 0, -H$.

The buoyancy frequency (N) is estimated from temperature and salinity profiles at moorings West, WB3, and EB, which are
converted into density profiles, $\rho(z)$, and averaged over the 2004 to 2018 time period:

210 $$N(z) = \sqrt{\frac{-g}{\rho_0}\frac{\partial\rho(z)}{\partial z}}$$ (8)

Normalisation is then computed to satisfy Kronecker delta, δ_{ij}, (rendering the resulting pressure modes dimensionless) such
that:

$$\int_{-H}^{0} F_i F_j dz = H\delta_{ij}$$ (9)

Where H is 4820 dbar, the bottom reference depth of the moorings.

215   The buoyancy frequency and the pressure modes, F_n (as per Eq. 6 and 7), are estimated at West, WB3 and EB (Fig. 4). The stratification profile is characteristic of buoyancy profiles in the North Atlantic (e.g. Szuts et al., 2012; Clément et al., 2014): in the west, the buoyancy frequency shows a sharp maximum at 80 dbar and a second maxima around 600 to 800 dbar before reaching zero at 1100 dbar. These two peaks indicate strong stratification linked to the seasonal and main pycnocline (Siegel et al., 1999). Moving eastward across the basin, at WB3, surface (upper 500 dbar) stratification decreases and deepens to 100

220   dbar, second peak also deepens and has slightly lower stratification than at mooring West. The stratification minima apparent in West and WB3 at 300-400 dbar is indicative of 18°C water (i.e. subtropical mode water), characteristic of the western subtropical North Atlantic. On the other side of the basin, in the eastern boundary, the stratification at EB is decreased though the subsurface maximum remains at 100 dbar.

Figure 4 also shows the first four pressure modes at West and WB3 and EB. Mode 0 is here representative of the barotropic

225   mode, while modes 1 to 3 are the first 3 baroclinic modes. The first mode shows a zero crossing roughly between 1000-1100 dbar in the western boundary (West and WB3), which deepens to 1500 dbar by the time it reaches the eastern boundary (EB). In general, western moorings show shallower zero crossings and more complex structure, reflective of the peaks in stratification in the west, compared to the eastern mooring which has a deeper zero crossing and smoother structure. The pressure modes shown here are consistent with the characteristic shape of known modes in the western North Atlantic (at this latitude) (e.g.

230   Gill, 1982; Szuts et al., 2012, their Fig. 6.14c and 2, respectively). The shape of the first baroclinic mode in the surface to its first zero crossing (1100-1500 dbar) will be key in informing the satellite-derived estimates of transport, as altimetry has been shown to capture the surface (0-1000 m) intensified structure flow (away from the boundaries by 45 km), reflective of the first baroclinic normal mode (Wunsch, 1997; Szuts et al., 2012). The zeroeth mode, i.e. the barotropic mode, is important in the deeper ocean (> 1000 m), which is less stratified (Wunsch, 1997; Kanzow et al., 2008). However, below the surface 1000 m,

235   changes in the deeper transport are not captured by satellite altimetry (Kanzow et al., 2008).

In the following sections, in-depth analysis of the normal modes from moorings and their relationship with satellite altimetry is explored.

4.3   Modal amplitude and variability

To understand the importance of each mode to the total variability observed in dynamic height anomaly, ϕ (Eq. 5, referenced

240   to 4820 dbar), measured by the RAPID moorings, the modal amplitude is analysed and used to construct time varying ϕ from the normal modes. The amplitudes of the modes, c_n, are estimated by integrating the product of the normal mode, F_n, and ϕ such that:

$$c_n(t) = \frac{1}{H} \int\limits_{-H}^{0} F_n(z)\phi(z,t)dz \tag{10}$$

where n = 0,1,2,3... is the mode number and H is the reference pressure 4820 dbar. Because satellite altimetry has been shown

245   to reflect fluctuations associated with the amplitude first baroclinic mode (Wunsch and Stammer, 1997; Hirschi et al., 2009),

the amplitude for the first mode, $c1$, can be estimated in terms of SLA, η, such that:

$$\hat{c}(t) = s \frac{g}{F_1(z=0)} \eta(t) \tag{11}$$

Where $F_1(z=0)$ is the surface value of the first mode, and s is a scale factor equal to 0.25, needed to adjust η to the correct magnitude. The scale factor was determined empirically by examining the signal from ϕ at the surface (z = 0) at moorings

250 West and EB against η. Fig. 5a shows the root mean square (RMS) of the surface $\phi(z=0)$ at West and EB, and the η (scaled by gravitational acceleration) along longitude at 26.125°N and 27.875°N over the 2004-2018 period. The RMS increases east to west at both latitudes. The RMS of η at eastern boundary is 0.18 $\mathrm{m^2 s^{-2}}$ at both 26.125°N and 27.875°N, compared with 0.08 $\mathrm{m^2 s^{-2}}$ observed at mooring EB. Moving west, the RMS values increase to a maximum of 0.70 $\mathrm{m^2 s^{-2}}$ at 74°W for η at 27.875°N, before quickly decreasing to 0.56 $\mathrm{m^2 s^{-2}}$ at 77°W (the longitude of the WB2 mooring). At 26.125°N, the RMS

255 values of η peak further west (75°W) up to 0.59 $\mathrm{m^2 s^{-2}}$, before decreasing to 0.39 $\mathrm{m^2 s^{-2}}$ at 77°W. The rapid decrease in RMS at the western boundary is likely due to the abrupt changes in topography in the region of the western Atlantic (Kanzow et al., 2009). At mooring West, the surface value of ϕ is 0.31 $\mathrm{m^2 s^{-2}}$, indicating a difference of 0.25 $\mathrm{m^2 s^{-2}}$ between ϕ at West and η at 27.875°N. In general, surface values of ϕ at West and EB show lower values when compared to both η at 26.125°N and 27.875°N. A scatterplot of the West and EB difference in the surface $\phi(z=0)$, $\Delta\phi$, and the east-west difference in η (where

260 η east is located at 27.875°N and 13.125°W and η west is at 27.87°N and 74.375°W, as per section 3.1), $\Delta\eta$, shows the slope of the regression line to be on the order of 0.25 and the intercept goes through the origin (1.3e-17) (Fig. 5b). In general, Fig. 5, shows the measure of the magnitude of the ϕ and the η time series. The comparison between $\phi(z=0)$ and η suggests that the satellite altimetry does not capture the full signal observed by the moorings. One of the reasons for this discrepancy may be due to the proximity of the moorings (e.g. WB2) to land, where variability experiences changes due to coastal processes

265 (Kanzow et al., 2009). The value of the slope of the regression line, i.e. 0.25, is thus used as the scale factor for the satellite where indicated (e.g. Eq. 11).

The modal amplitude, $\hat{c}$, computed from η (Eq. 11) is compared with the modal amplitude, c_n, computed from the first 3 baroclinic normal modes (Eq. 10) at West and EB (Fig. 6). The amplitude of the first mode, c_1, and $\hat{c}$ have a correlation of r = 0.57 (significant at 90% level) at West and a correlation of r = 0.67 (significant at 90% level) at EB. In the east (west),

270 $\hat{c}$ is constructed using η at 27.875°N and 13.125°W (27.875°N and 74.375°W). Comparison of c_1 and $\hat{c}$ time series shows a deviation in 2005-2006, where $\hat{c}$ has a larger negative anomaly (0.15 $\mathrm{m^2 s^{-2}}$) compared to c_1 (0.02 $\mathrm{m^2 s^{-2}}$); this is likely linked to the collapse of the WB2 mooring from November 2005 to March 2006 period, where WB3 mooring was used to fill the gap in the WB2 and West data. In general, all three modes start off with the same sign (negative) and eventually change sign (positive), suggesting longer term trends, with the exception of mode c_2 which starts positive. The modes have been defined/set

275 to positive at the surface. The higher modes, c_2 and c_3, have smaller amplitudes compared to c_1.

The modal amplitude (Eq. 10) can also be combined with the pressure modes (Eq. 7) to reconstruct ϕ as follows:

$$\phi_n^*(z,t) = c_n(t) F_n(z) \tag{12}$$

Fig. 7 shows the reconstructed ϕ, i.e. ϕ^*, using only the first baroclinic mode at West and EB as per Eq. (12) from the surface to the reference pressure 4820 dbar over the 2004 to 2018 period. The first baroclinic mode, ϕ_n^* for n = 1, at West shows a

280   general undulating pattern of negative and positive anomalies in the surface 1000 dbar: the anomalies are negative for years
       2007-2008, 2011, 2014, and positive during 2009, 2013, and from 2015 to 2017, similar to the surface anomalies observed
       in ϕ at West (Fig. 7a,b). The difference between ϕ and ϕ^* at West suggests that although the reconstruction generally captures
       a surface (1000 dbar) intensified structure, it underestimates the magnitude of ϕ and does not capture any of the signal below
       1000 dbar (Fig. 7c). These differences may be due to the fact that the reconstruction uses only the first baroclinic mode,
285   reflective of changes in the main thermocline, and thus has oversimplified structure in the upper layer of the ocean compared
       to the ϕ at West. Further, the baroclinic structure, in general, is more likely to reflect changes in the stratified upper ocean
       to roughly 1000 m, while in the deeper less stratified ocean, barotropic motion is more important (Kanzow et al., 2008). In
       the eastern boundary, ϕ^* is reconstructed using the first baroclinic mode at EB (Fig. 7d). The reconstruction captures similar
       negative and positive anomalies in the surface 1000 dbar to those observed in ϕ at EB (Fig. 7e). The magnitude of the ϕ
290   anomalies are generally substantially smaller at eastern part of the basin compared to the west.

       The contribution of the barotropic mode (mode 0) and higher baroclinic modes (modes 1 and 2) to ϕ^* is examined in Fig. 8.
       The inclusion of barotropic mode and higher baroclinic modes in ϕ^* shows substantially improved patterns of the ϕ variability
       in the upper 1000 dbar, with reduced differences at every pressure level (Fig. 8) compared to ϕ^* using only mode 1 (Fig. 7).
       To assess whether the inclusion of the barotropic and higher baroclinic modes makes a meaningful contribution to the upper
295   ocean transport, transports from the ϕ^* reconstruction using the normal modes and the ϕ at West and EB are presented in the
       following section.

4.4 Transport anomalies from West and EB moorings

Transport anomalies at West and EB are estimated using ϕ, ϕ^* and η respectively, with the aim of understanding the contribution
of the normal modes to ϕ variability and implications for satellite-based transport. Kanzow et al. (2010), Chidichimo et al.
300   (2010) and Szuts et al. (2012) set the precedent for estimating transport from a single mooring (as opposed to a horizontal
       gradient) to separate the contribution of the western and eastern components of the basinwide geostrophic transport. Therefore,
       transport from ϕ at West or EB mooring (as indicated) is defined as:

$$T'_\phi(t) = \frac{1}{f} \int_{-1100}^{0} \phi(z,t)dz \qquad (13)$$

The mode-reconstructed ϕ^* transport is calculated using the modes (Eq. 7) and modal amplitude (Eq. 10) such that:

305    $$T'_{F_n}(t) = \frac{1}{f} c_n(t) \int_{-1100}^{0} F_n(z)dz \qquad (14)$$

If the amplitude of the first mode is taken to correspond to η (i.e. $\hat{c}$; Eq. 11), then the satellite-based transport can be constructed
using the vertical structure from the first baroclinic mode F_1 in the following manner:

$$T'_\eta(t) = \frac{1}{f} \hat{c}_1(t) \int_{-1100}^{0} F_1(z)dz \qquad (15)$$

A comparison of the T_ϕ and the reconstructed T_F transports shows that T_F accounts for 83% of the variability of T_ϕ (r = 0.91,
310 statistically significant at 95% level) at West and 90% of the variance of T_ϕ (r = 0.95, statistically significant at 95% level) at
EB, where T_F is reconstructed using only the first mode (Fig. 9a,d). The satellite-based transport, T_η, on the other hand shows
lower correlation with T_ϕ at both West (r = 0.60, statistically significant at 90% level) and EB (r = 0.49, statistically significant
at 90% level). Though T_η captures the general patterns of variability observed in T_ϕ, there are several differences apparent
between T_η and T_ϕ occurring around 2005/06, which is when WB2 collapsed and data from WB3 was used instead; and
315 from 2004-2006 at EB. Additionally, the T_η time series generally appears to underestimate magnitude of the T_ϕ at West during
2009-2010, 2012 and 2016-2017 and at EB during 2010-2012, and 2016 (Fig. 9a,d). All three transport estimates show slowly
increasing trend over the 13 year period at West and EB. The results shown here are comparable to a satellite and RAPID
moorings comparison featured in Szuts et al. (2012, their Fig. 7).

Including the second baroclinic mode as well as the first in the reconstructed transport, T_F, shows some improvement in the
320 correlation with T_ϕ at West (r= 0.98, statistically significant at 95%) and slight decrease at EB (r= 0.94), though the amplitude
of T_F still underestimates T_ϕ (Fig. 9b,e). The addition of the barotropic mode to the first baroclinic mode in T_F noticeably
improves the amplitude of T_F and correlation with T_ϕ at West (r = 0.99) and EB (r = 1)(Fig. 9c,f). These results suggest that
the barotropic component plays a non-negligible role in the total variability and could explain some of the discrepancies in the
satellite-based estimates, as satellite altimetry typically only captures baroclinic variability.

325 The basinwide geostrophic transport can be constructed for ϕ and ϕ^* respectively, by integrating the east – west difference
such that Eq. (13) and (14) become:

$$T'_{\Delta\phi}(t) = \frac{1}{f} \int_{-1100}^{0} \phi_E(z,t) - \phi_W(z,t)dz \tag{16}$$

$$T'_{\Delta F_n}(t) = \frac{1}{f}[c_{nE}(t) \int_{-1100}^{0} F_{nE}(z)dz - c_{nW}(t) \int_{-1100}^{0} F_{nW}(z)dz] \tag{17}$$

330 Where subscripts E and W denote east (EB) and west (West), respectively. $T_{\Delta F}$ and $T_{\Delta\phi}(t)$ have a correlation of r = 0.91
(significant at 95% level) when $T_{\Delta F}$ is constructed using only mode 1 (Fig. 9g). The correlation between $T_{\Delta F}$ and $T_{\Delta\phi}(t)$
increases to r = 0.97, when $T_{\Delta F}$ is constructed using modes 1 and 2, and to r = 0.99 when $T_{\Delta F}$ is using modes 0 and 1
(Fig. 9h,i). These results suggest that the time-averaged first baroclinic mode accounts for most of the interior geostrophic
transport variability, and the remainder can be accounted for by the barotropic mode, reflective of changes in the deeper less
335 stratified ocean.

5   Construction of the GS, the UMO and AMOC transports

Principles of geostrophy are used again here to estimate T_{GS} from satellite altimetry. The east-west difference in η ($\Delta\eta$) in
the western end of the basin (i.e. west of 77°W) is compared with Gulf Stream transport anomalies from the submarine cable

data (Baringer and Larsen, 2001). Maximum correlation between T_{GS} from the cable data and the satellite $\Delta\eta$ (r = 0.70,
statistically significant at 95% level) is found when using η_E located at 27.625°N and 77.125°W, and η_W located at 27.625°N
and 80.125°W. Linear regression is used to obtain a final estimate for satellite-based GS transport:

$$T^*_{GS}(t) = [\eta_E - \eta_W]8 \tag{18}$$

The accuracy of T^*_{GS} was determined using a Monte-Carlo technique, where 90% of the time series was randomly sampled
10,000 times, performing a linear regression to obtain an upper and lower bound for the 90% confidence intervals. The satellite-
derived T^*_{GS} captures 49% of the variability of the in-situ T_{GS} and generally underestimates the amplitude of variability
(Fig. 10a,b). Similarly, a study by Volkov et al. (2020) used along-track satellite altimetry to infer T_{GS} measured at the level
of the Florida Straits, where they found that satellite altimetry captures 56% of variability observed from the T_{GS} estimated
from submarine cable records for the 2006-2020 time periods, where the cable-based transport estimates were subsampled at
10-day intervals to coincide with the along-track satellite passes.

The satellite-based T^*_{UMO} is constructed by combining the satellite-based mode amplitude, $\hat{c}$ (Eq. 11), with the first baro-
clinic mode, $F_1(z)$ (Eq. 7), as follows:

$$T^*_{UMO}(t) = \frac{1}{f}[\hat{c_E}(t)\int\limits_{-1100}^{0} F_E(z)dz - \hat{c_W}(t)\int\limits_{-1100}^{0} F_W(z)dz] \tag{19}$$

Where subscripts E and W denote east (for η_E at 27.875°N and 13.125°W and F_E at EB) and west (for η_W at 27.875°N and
74.375°W and F_W at West), respectively. The satellite-derived T^*_{UMO} is compared with RAPID T_{UMO} time series (r =0.75,
statistically significant at 95% level) in Fig. 10b. T^*_{UMO} follows the weakening apparent in the RAPID T_{UMO} in the year
2006 (positive anomalies indicate weakening in southward transport and viceversa), followed by the sharp intensification of
the southward flow reaching its maximum in 2009-2010. These changes in the transport have been previously documented
in Smeed et al. (2014, 2018), and in particular the 2008-2010 intensification in RAPID T_{UMO} is linked to strengthening of
southward circulation in the main thermocline (Smeed et al., 2014). In general, the satellite T^*_{UMO} follows the overall pattern
of variability measured by the T_{UMO}, capturing the weakening of southward flow in 2005-2006, 2011, and intensification
of southward flow in 2009-2010 and 2016-2017. However, the T^*_{UMO} does not capture the full extent of the RAPID T_{UMO}
intensification in 2009-2010 or in 2012 by approximately 1 Sv (Fig. 10c,d). Some of the missing variability may be linked to the
barotropic component not captured by satellite altimetry, as shown in the previous section (4.4). The 90% confidence interval
for T^*_{UMO} was estimated using a Monte-Carlo technique, where 90% of the $\Delta\eta$ timeseries is randomly sampled 10,000 times,
performing the regression with $\Delta\phi$ to acquire the scale factor as outlined in section 3.3, giving the upper and lower bounds for
the T^*_{UMO} calculation.

T^*_{MOC} is the sum of southward flow T^*_{UMO}, the Ekman transport, and northward-flowing T_{GS}. By incorporating the satellite-
derived T^*_{GS} as per Eq. (18) and the satellite-derived T^*_{UMO} as per Eq. (19), T^*_{MOC} can be defined by re-writing Eq. (1) such
that:

$$T^*_{MOC}(t) = T^*_{GS}(t) + T_{EK}(t) + T^*_{UMO}(t) \tag{20}$$

Where the Ekman transport (T_{EK}) is derived from ERA5 zonal wind stress as per the RAPID time series method. The satellite-constructed T^*_{MOC} and the RAPID T_{MOC} have a correlation of r = 0.83 (statistically significant at 95% level; Fig. 10e). T^*_{MOC} captures the start of the RAPID T_{MOC} in 2004, the weakening in 2005, the subsequent intensification in 2006, followed by the gradual weakening of RAPID T_{MOC} reaching a maximum low in 2010, and back to zero in 2011. In 2010 and 2013, the

375 T^*_{MOC} noticeably underestimates the magnitude (> 1 Sv) of the RAPID T_{MOC} fluctuations. The anomalously low event in T_{UMO} during 2009-2010 is attributed to anomalous wind-driven Ekman transport (Roberts et al., 2013; Zhao and Johns, 2014). After the 2009-2010 event, the AMOC recovers and appears to show a positive tendency. The gradual increase in the T_{MOC} apparent from 2010 onwards, however, has not yet been shown to be statistically significant at 26°N (Moat et al., 2020b).

The satellite-derived T^*_{UMO} and T^*_{MOC} were also computed with a time varying $F_1(z,t)$ with almost no improvement: the

380 correlation between T^*_{UMO}, using a time-varying F_1, and the RAPID T_{UMO} increased slightly from r = 0.75 to r = 0.76, and for T^*_{MOC} and RAPID T_{MOC} there was no change (i.e. r = 0.83). This suggests that AMOC variability can be estimated from surface geostrophic velocity and the time-averaged vertical structure of the flow.

6   Construction of volume transport from historical altimetry data

TOPEX/Poseidon was one of the first satellite altimetry missions to be launched with a major oceanographic focus (Fu et al.,

385 1994); since its launch in 1992, it has provided an invaluable source of measurements for studying surface ocean circulation (e.g. Willis, 2010; Frajka-Williams, 2015). In this section, the T^*_{UMO} and the T^*_{MOC} are constructed for the full available satellite time period, 1993 to 2018 (full annual coverage in the satellite data for the product used here starts in January 1993), yielding 11 years of data that pre-date the RAPID mooring array.

Previously, satellite-derived estimates of the T_{UMO} and the T_{MOC} have been compared with the RAPID 26°N array, and

390 constructed for the 1993 to 2013 period in Frajka-Williams (2015, hereafter EFW15). EFW15 found that SLA could be used to obtain a proxy for mass overturning transport. The statistical relationship between the RAPID T_{UMO} and the SLA on low frequency (18 month) timescales provided the main method for estimating the EFW15 T_{UMO}. The EFW15 T_{MOC} was estimated by adding the same estimates of T_{EK} (ERA-Interim) and T_{GS} (submarine cable) used by RAPID to the T_{UMO}. Here it is fitting to compare the EFW15 method with the method derived in sections 4 and 5, which relies on altimetric data and

395 geostrophic balance, and therefore has the potential to provide a more physically robust method for monitoring the meridional overturning circulation and could be extended to other latitudes in the Atlantic. Additionally, the RAPID T_{MOC} is compared with a third separate T_{MOC} estimated from GloSea5, a global ocean and ice reanalysis product (Blockley et al., 2014; Jackson et al., 2019; MacLachlan et al., 2015). GloSea5 uses the ocean model NEMO (Nucleus for European Modelling of the Ocean) that has a $\frac{1}{4}^\circ$ ocean resolution and assimilates observational data including satellite (Megann et al., 2014). The GloSea5 T_{MOC}

400 estimates at 26°N are averaged monthly (further details on GloSea5 described in Jackson et al. (2019)). As in previous sections, annual seasonal climatology is removed from each time series and an 18-month Gaussian filter is applied (with the exception of the EFW15 time series which uses an 18-month Tukey filter). Since the overlap between the RAPID array data and the

EFW15 time series spans 2004 to 2013 only, all correlations presented in this section reflect the r-value for the 2004 to 2013
time period.

405   The T^*_{UMO} and the EFW15 T_{UMO} are first compared with the RAPID T_{UMO} time series in Fig. 11a. Over the 2004 to 2013
time period, the T^*_{UMO} and EFW15 T_{UMO} have correlations of r = 0.79 and r = 0.85 (statistically significant at 90% level),
respectively with the RAPID T_{UMO} time series. Both time series capture the RAPID T_{UMO} weakening in 2005-2006 (positive
anomalies indicate weakening in southward transport and viceversa), 2010-2011 and the strengthening in 2009-2010 and 2013
(Fig. 11a). Both the T^*_{UMO} and EFW15 T_{UMO} underestimate the 2009-2010 intensification observed by the RAPID T_{UMO}.
410 In the time period pre-dating the RAPID programme, EFW15 T_{UMO} shows a weakening in 1995 and 2001, and intensification
in 1999 and 2004 of the southward flow. In comparison, the T_{UMO} shows lower amplitude variability but a higher southward
transport in the 1993-2003 time period. The EFW15 T_{UMO} is centered on a single SLA point in the western end of the basin at
70°W and 30°N, while in the satellite estimate derived here, T^*_{UMO}, is based on the difference in SLA in the east at 13.125°W
and 27.875°N and west at 74.375°W and 27.875°N (i.e. variability in the eastern end of the basin is taken into account as well).
415 Thus holding the eastern component of the T^*_{UMO} constant highlights its contribution to total T^*_{UMO} variability, which in the
pre-RAPID time period acts to strengthen the mean T^*_{UMO} southward transport; in other words, holding the eastern component
constant leads to a weakening in southward transport that suggests improved agreement with the magnitude of EFW15 T_{UMO}
(Fig. 11a).

The T^*_{MOC}, EFW15 T_{MOC}, and GloSea5 T_{MOC} are compared to the RAPID T_{MOC} over the 2004-2013 time period
420 (Fig. 11b). The T^*_{MOC} has the highest correlation with the RAPID T_{MOC} (r = 0.87, statistically significant at 95% level)
while EFW15 T_{MOC} and GloSea5 T_{MOC} show slightly lower correlations with the RAPID T_{MOC} (r = 0.84 and r = 085,
respectively, statistically significant for at least 90% level). The GloSea5 T_{MOC} proxy underestimates the T_{MOC} mean values
in the 2004 to 2010, and does not capture the weakening of southward flow apparent in the RAPID T_{MOC} in 2005-2006
(Fig. 11b). In the pre-RAPID time period, 1993-2003, there is surprisingly little agreement between the T_{MOC} proxies. All
425 three T_{MOC} reconstructions show a weakening in the southward flow in 1996 or 1997, followed by an intensification toward
the late 90s. This general mid-to-late 90s strengthening is in agreement with changes in the Atlantic Multidecadal Variability
phase, which was marked by a positive phase in the late 1990s (Zhang et al., 2019). In 2003-2004, GloSea5 T_{MOC} and T^*_{MOC}
show a weakening closer to the T_{MOC} values at the start of the RAPID programme, which is not captured by the EFW15
T_{MOC}. In general, it is difficult to determine which of the three T_{MOC} reconstructions might provide a best estimate of the
430 observed T_{MOC} over the 1993-2004 time period. For instance, the correlations between each T_{MOC} reconstruction and RAPID
T_{MOC} are very similar, however there is poor agreement between the three T_{MOC} reconstructions in the time period pre-dating
RAPID. Further investigation is therefore needed to confidently reconstruct the MOC for the 1993 to 2003 time period.

7   Summary and conclusions

Mooring array programmes such as the RAPID 26°N array have made step-change advancements in our understanding of the
435 AMOC; however they are limited to measurements at a single latitude and alone cannot be used to infer upstream/downstream

changes in the larger scale structure of the AMOC. Mooring arrays are also a single point of failure should the moorings collapse. In light of the increase in studies linking the AMOC to climate impacts (Zhang et al., 2019), it is now more important than ever to find long term and cost-effective replacements/backup systems that can monitor changes in the AMOC. In this study, the vertical structure of the flow from RAPID moorings is examined in detail and combined with satellite altimetry to
440   design and test a new method for estimating AMOC variability. We find that:

- Analysis of the normal modes from RAPID mooring data shows that the first baroclinic mode accounts for 83% of the observed interior geostrophic transport variability, and the remaining variability can be accounted for by barotropic motion,

- Comparison between dynamic height anomaly from the RAPID moorings and satellite altimetry indicate that satellite
445   altimetry does not completely capture the mean sea surface signal observed by the RAPID moorings, hence it is necessary to apply a scale factor (0.25) to SLA in order to correctly compute satellite-derived transport estimates,

- A satellite-derived Gulf Stream transport, T_{GS}^*, is computed using linear regression. T_{GS}^* has a correlation of r = 0.70 (statistically significant at 95% level) with a submarine cable time series,

- Principles of geostrophy and Rossby wave theory are used to devise a new method for constructing the upper mid-ocean
450   transport, T_{UMO}^*, and by extension the T_{MOC}^*, at 26°N from satellite altimetry on low frequency (18 months) time scales. The first baroclinic mode, derived from time-averaged density profiles, is combined with SLA to reproduce the T_{UMO}^* and T_{MOC}^* transports, which provide a reasonably good reproduction of the RAPID upper mid-ocean and AMOC transport (r = 0.75 and r = 0.83, respectively). It was also shown that time-varying vertical modes do not necessarily improve correlation between the RAPID T_{MOC} and the satellite-derived T_{MOC}^*,

455   - Finally, the satellite-derived T_{UMO}^* and T_{MOC}^* are reconstructed for the the full satellite period (1993 to 2018). The 26-year reconstructions of T_{UMO}^* and T_{MOC}^* were compared with another separate satellite-derived proxy (EFW15) and a T_{MOC} reconstruction from the GloSea5 reanalysis. Though all reconstructions had correlations of at least r = 0.79 with RAPID-based transports for the 2004 to 2013 time period, the 1993-2003 time period showed poor agreement between the three T_{MOC} reconstructions, suggesting further studies are needed to confidently reproduce the fluctuations in the
460   AMOC during times pre-dating the RAPID programme.

Methods developed here aim to provide a new dynamically-based technique for estimating changes in the AMOC from satellite altimetry at 26°N and lay the groundwork for developing future methods that could provide continuous monitoring of AMOC across other latitudes in the north Atlantic.

Data availability. The RAPID-MOCHA-WBTS time series (Moat et al., 2020a) is available at https://doi.org/10.5285/aa57e879-4cca-28b6-
465   e053-6c86abc02de5.

Copernicus Marine Environment Monitoring Service for data access available online: http://marine.copernicus.eu/services-portfolio/access-to-products/ product id = SEALEVEL_GLO_PHY_L4_REP_OBSERVATIONS_008_047.

ERA5 wind stress is available via https://cds.climate.copernicus.eu/cdsapp#!/home (Copernicus Climate Change Service, 2020). The Gulf Stream cable data is available via https://www.aoml.noaa.gov/phod/floridacurrent/index.php. The GloSea5 time series is available from

470 Jackson et al., (2019) upon request.

Author contributions. ASF wrote the manuscript with input/contributions from all authors. ASF, EFW, DAS, BIM contributed to the analysis. EFW, BIM, DAS contributed to data collection/provided processed data.

Competing interests. The authors declare that they have no conflict of interest.

Acknowledgements. The authors thank the many officers, crews and technicians who helped to collect these data. ASF also thanks L. Clement

475 for helpful discussions on normal mode decomposition.

References

Baringer, M. O. and Larsen, J. C.: Sixteen years of Florida Current transport at 27 N, Geophysical Research Letters, 28, 3179–3182, 2001.

Bingham, R. J. and Hughes, C. W.: Geostrophic dynamics of meridional transport variability in the subpolar North Atlantic, Journal of Geophysical Research: Oceans, 114, 2009.

480 Blockley, E. W., Martin, M. J., McLaren, A. J., Ryan, A. G., Waters, J., Lea, D. J., Mirouze, I., Peterson, K. A., Sellar, A., and Storkey, D.: Recent development of the Met Office operational ocean forecasting system: an overview and assessment of the new Global FOAM forecasts., Geoscientific Model Development, 7, 2014.

Bryden, H. L., Mujahid, A., Cunningham, S. A., and Kanzow, T.: Adjustment of the basin-scale circulation at 26 degrees N to variations in gulf stream, deep western boundary current and Ekman transports as observed by the rapid array, Ocean Science, 5, 421–433, 2009.

485 Caesar, L., Rahmstorf, S., Robinson, A., Feulner, G., and Saba, V.: Observed fingerprint of a weakening Atlantic Ocean overturning circulation, Nature, 556, 191–196, 2018.

Chelton, D. B., Schlax, M. G., Samelson, R. M., and de Szoeke, R. A.: Global observations of large oceanic eddies, Geophysical Research Letters, 34, 2007.

Chidichimo, M., Kanzow, T., Cunningham, S., Johns, W., and Marotzke, J.: The contribution of eastern-boundary density variations to the
490 Atlantic meridional overturning circulation at 26.5 N, Ocean Science, 6, 475–490, 2010.

Clément, L., Frajka-Williams, E., Szuts, Z. B., and Cunningham, S. A.: Vertical structure of eddies and R ossby waves, and their effect on the A tlantic meridional overturning circulation at 26.5° N, Journal of Geophysical Research: Oceans, 119, 6479–6498, 2014.

Emery, W. J. and Thomson, R. E.: Time-series analysis methods, Data analysis methods in physical oceanography, 371, 2001.

Evans, D. G., Toole, J., Forget, G., Zika, J. D., Naveira Garabato, A. C., Nurser, A. J. G., and Yu, L.: Recent Wind-Driven Variabil-
495 ity in Atlantic Water Mass Distribution and Meridional Overturning Circulation, Journal of Physical Oceanography, 47, 633–647, https://doi.org/10.1175/JPO-D-16-0089.1, https://doi.org/10.1175/JPO-D-16-0089.1, 2017.

Frajka-Williams, E., Ansorge, I. J., Baehr, J., Bryden, H. L., Chidichimo, M. P., Cunningham, S. A., Danabasoglu, G., Dong, S., Donohue, K. A., and Elipot, S.: Atlantic meridional overturning circulation: Observed transport and variability, Frontiers in Marine Science, 6, 260, 2019.

500 Frajka-Williams, E.: Estimating the Atlantic overturning at 26 N using satellite altimetry and cable measurements, Geophysical Research Letters, 42, 3458–3464, 2015.

Fu, L., Christensen, E. J., Yamarone, C. A., Lefebvre, M., Menard, Y., Dorrer, M., and Escudier, P.: TOPEX/POSEIDON mission overview, Journal of Geophysical Research: Oceans, 99, 24 369–24 381, 1994.

Gill, A. E.: Atmosphere-Ocean dynamics (International Geophysics Series), academic press, 1982.

505 Hall, M. M. and Bryden, H. L.: Direct estimates and mechanisms of ocean heat transport, Deep Sea Research Part A. Oceanographic Research Papers, 29, 339–359, 1982.

Hersbach, H., Bell, B., Berrisford, P., Hirahara, S., Horányi, A., Muñoz-Sabater, J., Nicolas, J., Peubey, C., Radu, R., and Schepers, D.: The ERA5 global reanalysis, Quarterly Journal of the Royal Meteorological Society, 146, 1999–2049, 2020.

Hirschi, J. J. M., Killworth, P. D., and Blundell, J. R.: Subannual, seasonal, and interannual variability of the North Atlantic meridional
510 overturning circulation, Journal of Physical Oceanography, 37, 1246–1265, 2007.

Hirschi, J. J. M., Killworth, P. D., Blundell, J. R., and Cromwell, D.: Sea surface height signals as indicators for oceanic meridional mass transports, Journal of Physical Oceanography, 39, 581–601, 2009.

Jackson, L. C., Dubois, C., Forget, G., Haines, K., Harrison, M., Iovino, D., Köhl, A., Mignac, D., Masina, S., Peterson, K. A., Piecuch, C. G., Roberts, C. D., Robson, J., Storto, A., Toyoda, T., Valdivieso, M., Wilson, C., Wang, Y., and Zuo, H.: The Mean State and Variability of the North Atlantic Circulation: A Perspective From Ocean Reanalyses, Journal of Geophysical Research: Oceans, 124, 9141–9170, https://doi.org/https://doi.org/10.1029/2019JC015210, https://doi.org/10.1029/2019JC015210, 2019.

Johnson, H. L. and Marshall, D. P.: A theory for the surface Atlantic response to thermohaline variability, Journal of Physical Oceanography, 32, 1121–1132, 2002.

Kanzow, T., Send, U., and McCartney, M.: On the variability of the deep meridional transports in the tropical North Atlantic, Deep Sea Research Part I: Oceanographic Research Papers, 55, 1601–1623, 2008.

Kanzow, T., Johnson, H. L., Marshall, D. P., Cunningham, S. A., Hirschi, J.-M., Mujahid, A., Bryden, H. L., and Johns, W. E.: Basinwide integrated volume transports in an eddy-filled ocean, Journal of Physical Oceanography, 39, 3091–3110, 2009.

Kanzow, T., Cunningham, S. A., Johns, W. E., Hirschi, J. J. M., Marotzke, J., Baringer, M. O., Meinen, C. S., Chidichimo, M. P., Atkinson, C., and Beal, L. M.: Seasonal variability of the Atlantic meridional overturning circulation at 26.5 N, Journal of Climate, 23, 5678–5698, 2010.

Killworth, P. D. and Blundell, J. R.: Long extratropical planetary wave propagation in the presence of slowly varying mean flow and bottom topography. Part II: Ray propagation and comparison with observations, Journal of physical oceanography, 33, 802–821, 2003.

MacLachlan, C., Arribas, A., Peterson, K. A., Maidens, A., Fereday, D., Scaife, A. A., Gordon, M., Vellinga, M., Williams, A., and Comer, R. E.: Global Seasonal forecast system version 5 (GloSea5): A high-resolution seasonal forecast system, Quarterly Journal of the Royal Meteorological Society, 141, 1072–1084, 2015.

McCarthy, G. D., Smeed, D. A., Johns, W. E., Frajka-Williams, E., Moat, B. I., Rayner, D., Baringer, M. O., Meinen, C. S., Collins, J., and Bryden, H. L.: Measuring the Atlantic meridional overturning circulation at 26 N, Progress in Oceanography, 130, 91–111, 2015.

Megann, A. P., Storkey, D., Aksenov, Y., Alderson, S., Calvert, D., Graham, T., Hyder, P., Siddorn, J., and Sinha, B.: Go 5.0: The joint NERC-Met office NEMO global ocean model for use in coupled and forced applications, Geotechnical Model Development, 7, 1069–1092, 2014.

Moat, B. I., Frajka-Williams, E., Smeed, D., Rayner, D., Sanchez-Franks, A., Johns, W. E., Baringer, M. O., Volkov, D., and Collins, J.: Atlantic meridional overturning circulation observed by the RAPID-MOCHA-WBTS (RAPID-Meridional Overturning Circulation and Heatflux Array-Western Boundary Time Series) array at 26N from 2004 to 2018 (v2018.2), British Oceanographic Data Centre, National Oceanography Centre, NERC, UK., https://doi.org/10.5285/aa57e879-4cca-28b6-e053-6c86abc02de5, 2020a.

Moat, B. I., Smeed, D. A., Frajka-Williams, E., Desbruyères, D. G., Beaulieu, C., Johns, W. E., Rayner, D., Sanchez-Franks, A., Baringer, M. O., and Volkov, D.: Pending recovery in the strength of the meridional overturning circulation at 26° N, Ocean Science, 16, 863–874, 2020b.

Pohlmann, A., Fricke, W. F., Reinecke, F., Kusian, B., Liesegang, H., Cramm, R., Eitinger, T., Ewering, C., Pötter, M., and Schwartz, E.: Genome sequence of the bioplastic-producing "Knallgas" bacterium Ralstonia eutropha H16, Nature biotechnology, 24, 1257–1262, 2006.

Rayner, D., Hirschi, J. J.-M., Kanzow, T., Johns, W. E., Wright, P. G., Frajka-Williams, E., Bryden, H. L., Meinen, C. S., Baringer, M. O., and Marotzke, J.: Monitoring the Atlantic meridional overturning circulation, Deep Sea Research Part II: Topical Studies in Oceanography, 58, 1744–1753, 2011.

Roberts, C. D., Waters, J., Peterson, K. A., Palmer, M. D., McCarthy, G. D., Frajka-Williams, E., Haines, K., Lea, D. J., Martin, M. J., Storkey, D., Blockley, E. W., and Zuo, H.: Atmosphere drives recent interannual variability of the Atlantic meridional overturning circulation at 26.5°N, Geophysical Research Letters, 40, 5164–5170, https://doi.org/https://doi.org/10.1002/grl.50930, https://doi.org/10.1002/grl.50930, 2013.

Sanchez-Franks, A. and Zhang, R.: Impact of the Atlantic meridional overturning circulation on the decadal variability of the Gulf Stream path and regional chlorophyll and nutrient concentrations, Geophysical Research Letters, https://doi.org/10.1002/2015GL066262, http://www.scopus.com/inward/record.url?eid=2-s2.0-84956958293{&}partnerID=MN8TOARS, 2015.

555 Sanchez-Franks, A., Hameed, S., and Wilson, R. E.: The Icelandic low as a predictor of the Gulf Stream north wall position, Journal of Physical Oceanography, https://doi.org/10.1175/JPO-D-14-0244.1, http://www.scopus.com/inward/record.url?eid=2-s2.0-84961615534{&}partnerID=MN8TOARS, 2016.

Siegel, D. A., McGillicuddy Jr, D. J., and Fields, E. A.: Mesoscale eddies, satellite altimetry, and new production in the Sargasso Sea, Journal of Geophysical Research: Oceans, 104, 13 359–13 379, 1999.

Smeed, D. A., McCarthy, G. D., Cunningham, S. A., Frajka-Williams, E., Rayner, D., Johns, W. E., Meinen, C. S., Baringer, M. O., Moat,
560 B. I., and Duchez, A.: Observed decline of the Atlantic meridional overturning circulation 2004–2012, Ocean Science, 10, 29–38, 2014.

Smeed, D. A., Josey, S. A., Beaulieu, C., Johns, W. E., Moat, B. I., Frajka-Williams, E., Rayner, D., Meinen, C. S., Baringer, M. O., and Bryden, H. L.: The North Atlantic Ocean is in a state of reduced overturning, Geophysical Research Letters, 45, 1527–1533, 2018.

Srokosz, M., Baringer, M., Bryden, H., Cunningham, S., Delworth, T., Lozier, S., Marotzke, J., and Sutton, R.: Past, present, and future changes in the Atlantic meridional overturning circulation, Bulletin of the American Meteorological Society, 93, 1663–1676, 2012.

565 Szuts, Z. B., Blundell, J. R., Chidichimo, M. P., and Marotzke, J.: A vertical-mode decomposition to investigate low-frequency internal motion across the Atlantic at 26 N, Ocean Science, 8, 345–367, 2012.

Trenberth, K. E. and Caron, J. M.: Estimates of meridional atmosphere and ocean heat transports, Journal of Climate, 14, 3433–3443, 2001.

Volkov, D. L., Domingues, R., Meinen, C. S., Garcia, R., Baringer, M., Goni, G., and Smith, R. H.: Inferring Florida Current volume transport from satellite altimetry, Journal of Geophysical Research: Oceans, n/a, e2020JC016 763,
570 https://doi.org/https://doi.org/10.1029/2020JC016763, https://doi.org/10.1029/2020JC016763, 2020.

Willis, J. K.: Can in situ floats and satellite altimeters detect long-term changes in Atlantic Ocean overturning?, Geophysical research letters, 37, 2010.

Wunsch, C.: The vertical partition of oceanic horizontal kinetic energy, Journal of Physical Oceanography, 27, 1770–1794, 1997.

Wunsch, C. and Stammer, D.: Atmospheric loading and the oceanic "inverted barometer" effect, Reviews of Geophysics, 35, 79–107, 1997.

575 Zhang, R.: Coherent surface-subsurface fingerprint of the Atlantic meridional overturning circulation, Geophysical Research Letters, 35, 2008.

Zhang, R., Sutton, R., Danabasoglu, G., Kwon, Y., Marsh, R., Yeager, S. G., Amrhein, D. E., and Little, C. M.: A review of the role of the Atlantic meridional overturning circulation in Atlantic multidecadal variability and associated climate impacts, Reviews of Geophysics, 57, 316–375, 2019.

580 Zhao, J. and Johns, W.: Wind-forced interannual variability of the Atlantic Meridional Overturning Circulation at 26.5°N, Journal of Geophysical Research: Oceans, 119, 2403–2419, https://doi.org/https://doi.org/10.1002/2013JC009407, https://doi.org/10.1002/2013JC009407, 2014.
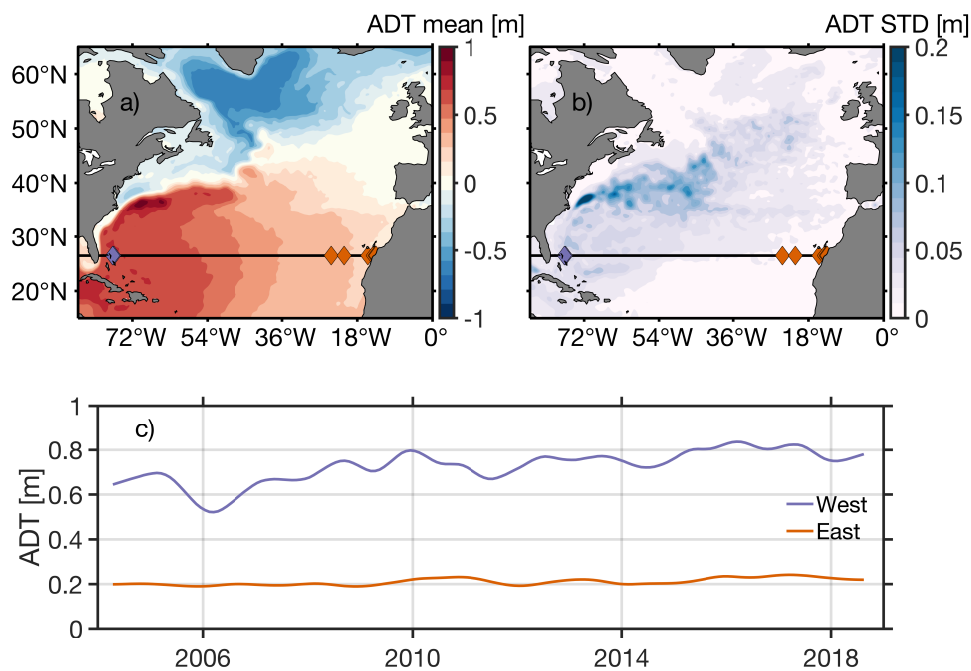
Figure 1. Absolute Dynamic Topography (ADT) (a) mean and (b) standard deviation (STD) across the North Atlantic over 2004 to 2018 time period. Western (purple diamonds) and eastern (orange diamonds) moorings are indicated along the RAPID array (black line). (c) Time series of the western (purple line) and eastern (orange line) ADT near the locations of the western (WB2, WB3) and eastern moorings (EB), respectively. Units in m.
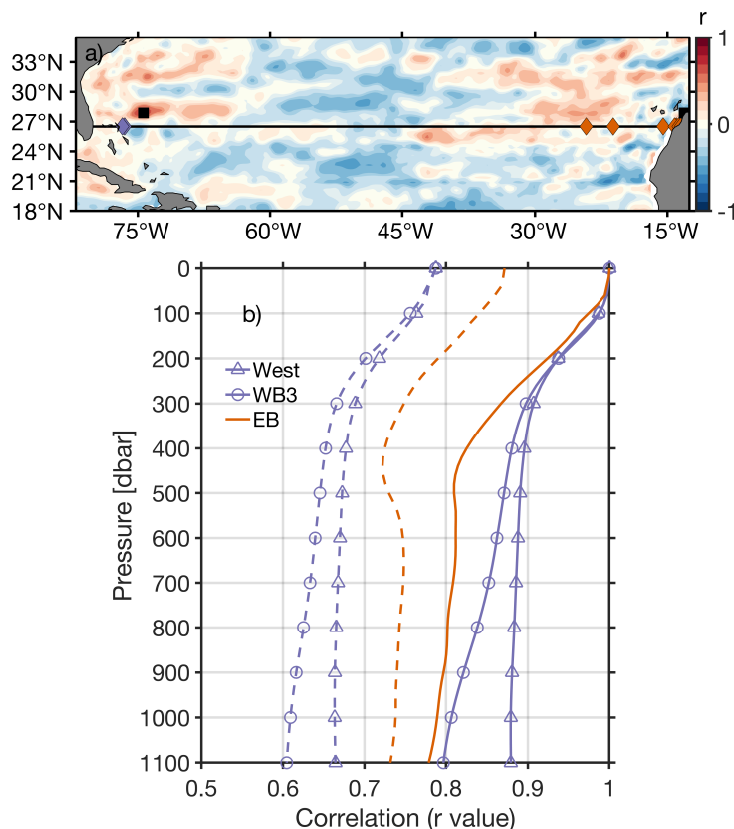
Figure 2. a) Correlation map between east-west difference in SLA ($\Delta\eta$) and the RAPID upper mid-ocean transport (T_{UMO}). Black squares in the western and eastern part of basin indicate region of maximum correlation between $\Delta\eta$ and T_{UMO}. Western (purple diamonds) and eastern (orange diamonds) moorings are indicated along the RAPID array (black line). b) Correlation between SLA and dynamic height from RAPID moorings West (purple circle line), WB3 (purple triangle line), and EB (orange solid line) at each pressure. Dynamic height from RAPID moorings is referenced to SLA at the surface. The dashed lines indicate the 95% significance level for SLA and dynamic height r-values per mooring using the two-tailed t test.
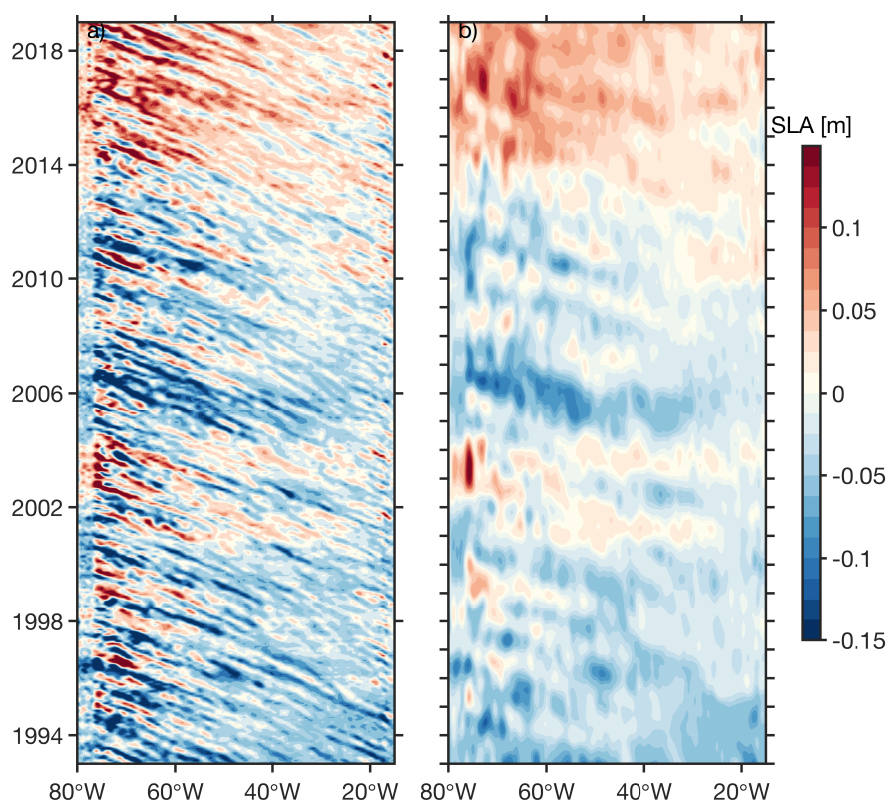
Figure 3. Hovmoller of sea level anomaly (SLA) at 26.625°N over 1993 to 2018 for monthly resolution (a) and 18-month smoothed (b). Units in m.
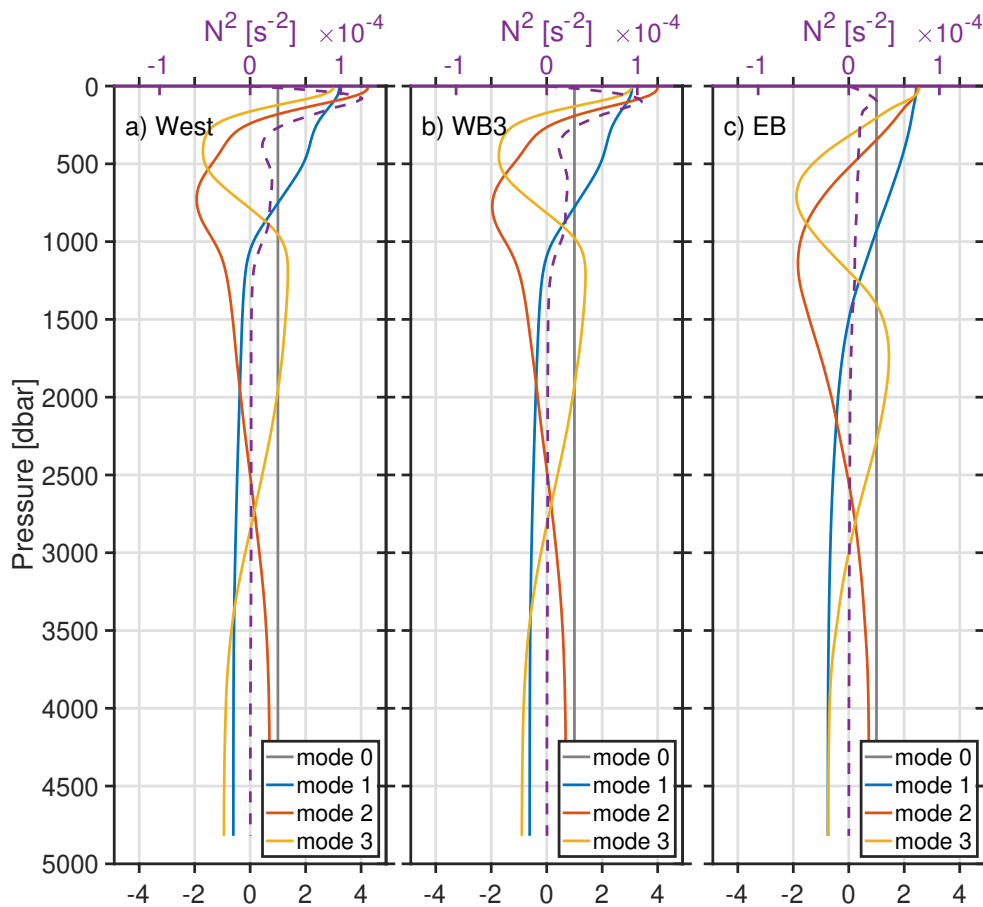
Figure 4. The buoyancy frequency (N^2; dashed purple line) and the horizontal velocity normal modes: the barotropic mode (i.e. mode 0; grey line) and the baroclinic normal mode 1 (blue line), mode 2 (orange line) and mode 3 (yellow line) at RAPID moorings: a) West, b) WB3, and c) EB. The modes have been normalised to satisfy Eq. (9) and are dimensionless.
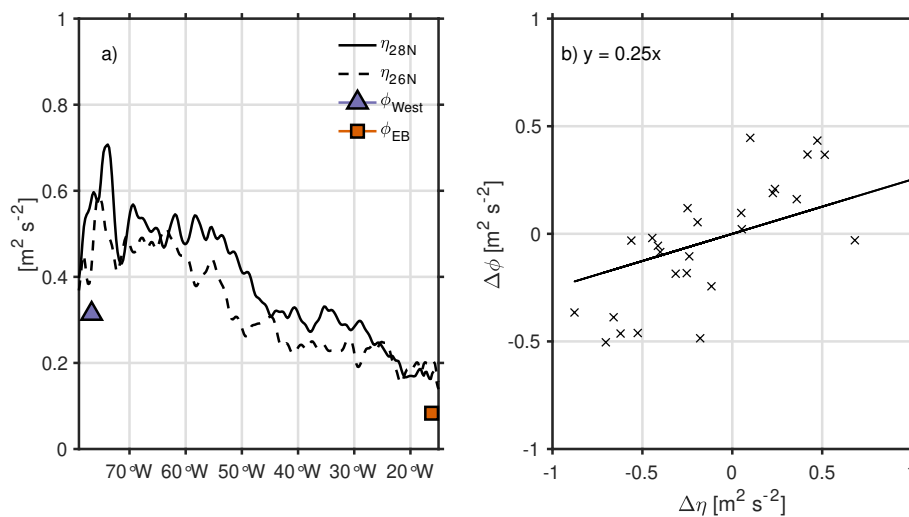
Figure 5. (a) The root mean square (RMS) at every longitude point of the SLA (η) at 26.125°N (black dashed line; latitude of RAPID moorings) and at 27.875°N (black solid line; latitude of maximum correlation between $\Delta\eta$ and T_{UMO} − see Fig. 2). Symbols indicate the RMS of the dynamic height anomaly (ϕ) at the surface ($z = 0$) at West (purple triangle) and EB (orange square) moorings. (b) Scatterplot of the east-west difference in η, i.e. $\Delta\eta$, vs east (EB) – west (West) difference in the ϕ, i.e. $\Delta\phi$. In (b) data are subsampled once every 6 months. In both plots, η is scaled by gravitational acceleration. Units in m²s⁻².
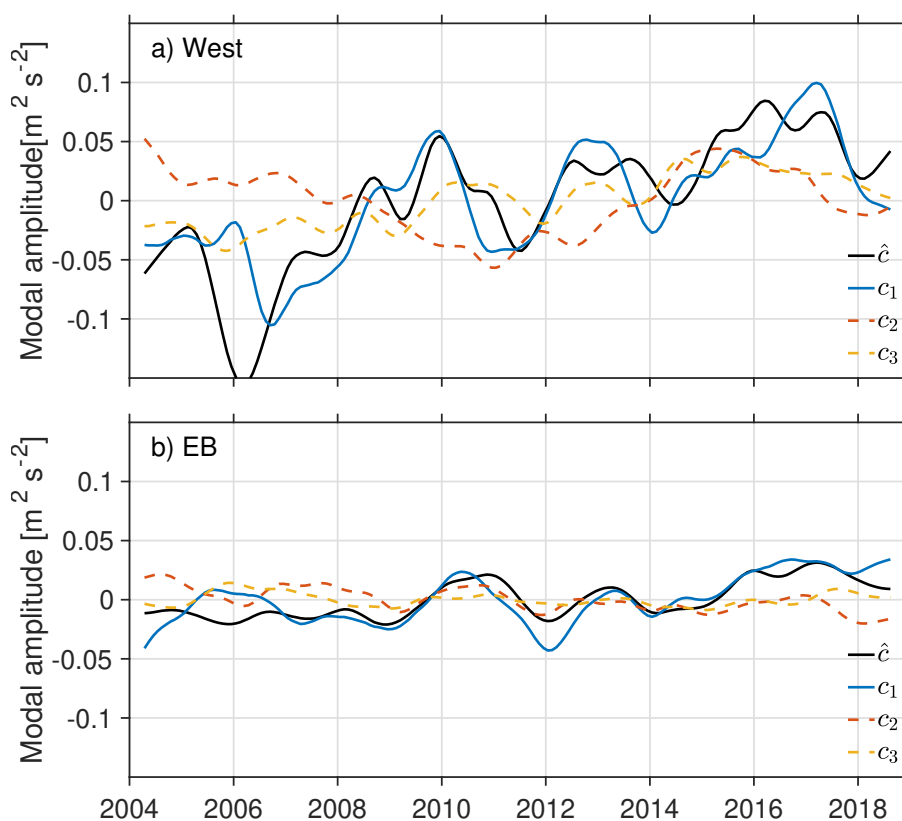
Figure 6. Modal amplitudes, c_n, fit to the dynamic height anomaly (ϕ) and the baroclinic modes, F_n, as per Eq. (10) at (a) West and (b) EB moorings. The first three modal amplitudes: c_1 (blue line), c_2 (orange dashed line), and c_3 (yellow dashed line) are compared with first mode amplitude estimated from SLA, $\hat{c}$ (black line) as per Eq. (11). Units in $\mathrm{m^2 s^{-2}}$.
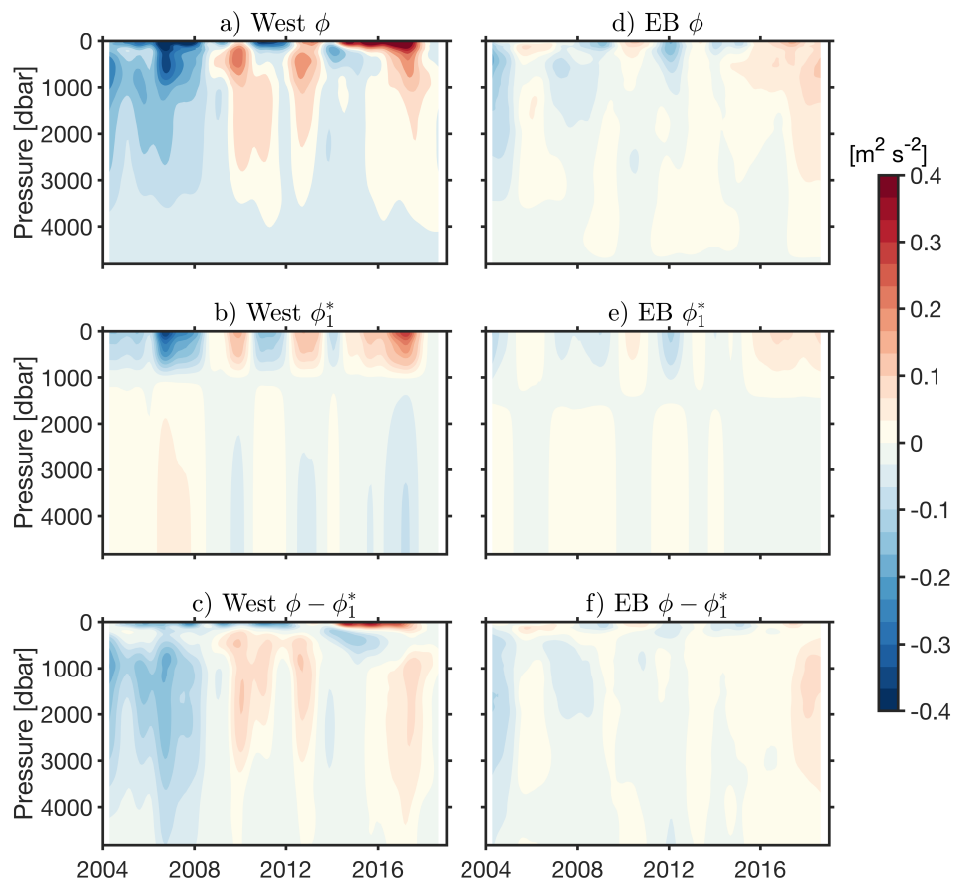
Figure 7. Dynamic height anomaly (ϕ) from the surface to the reference pressure 4820 dbar over the 2004 to 2018 period from RAPID moorings at West (a) and EB (d). Reconstruction of the dynamic height anomaly (ϕ^*) at West (b) and EB (e) using the first baroclinic mode (F_1) and the corresponding modal amplitude (c_1) as per Eq. (12). The difference between the ϕ^* for the first baroclinic mode and ϕ at West (c) and EB (f). Units in $\mathrm{m^2 s^{-2}}$.
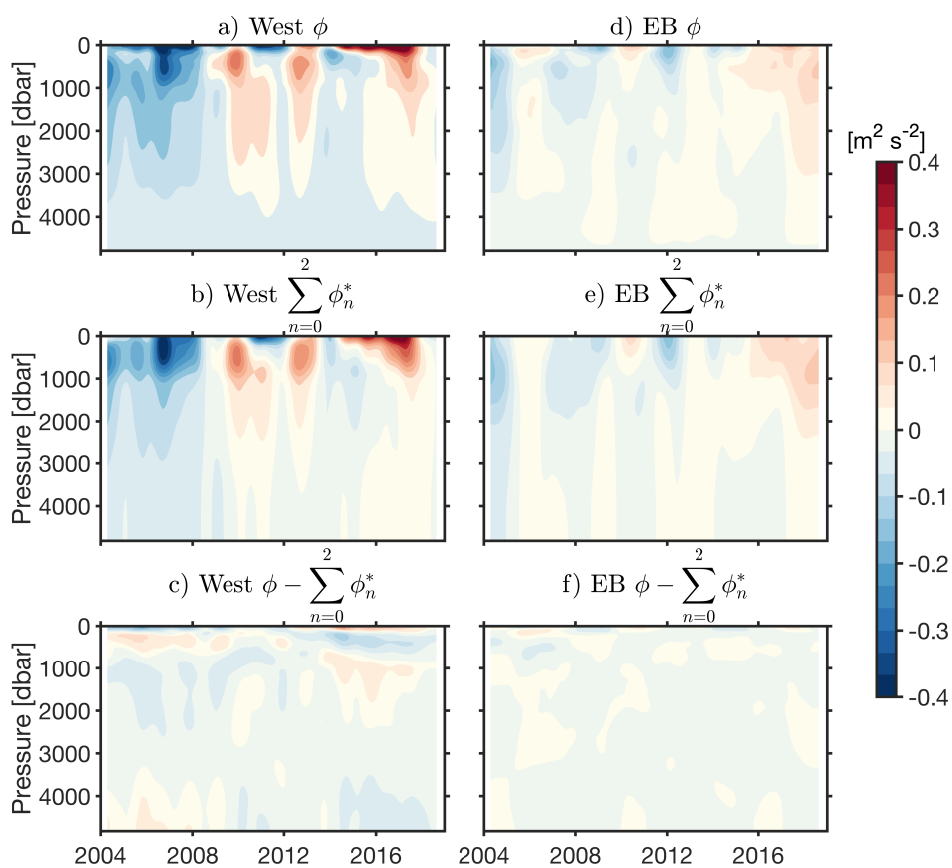
Figure 8. Same as in Fig. 7, except the contribution of the barotropic mode ($n = 0$) and the first two baroclinic modes ($n = 0, 1, 2$) are included in the dynamic height anomaly reconstruction (ϕ^*) at West (b) and EB (e).
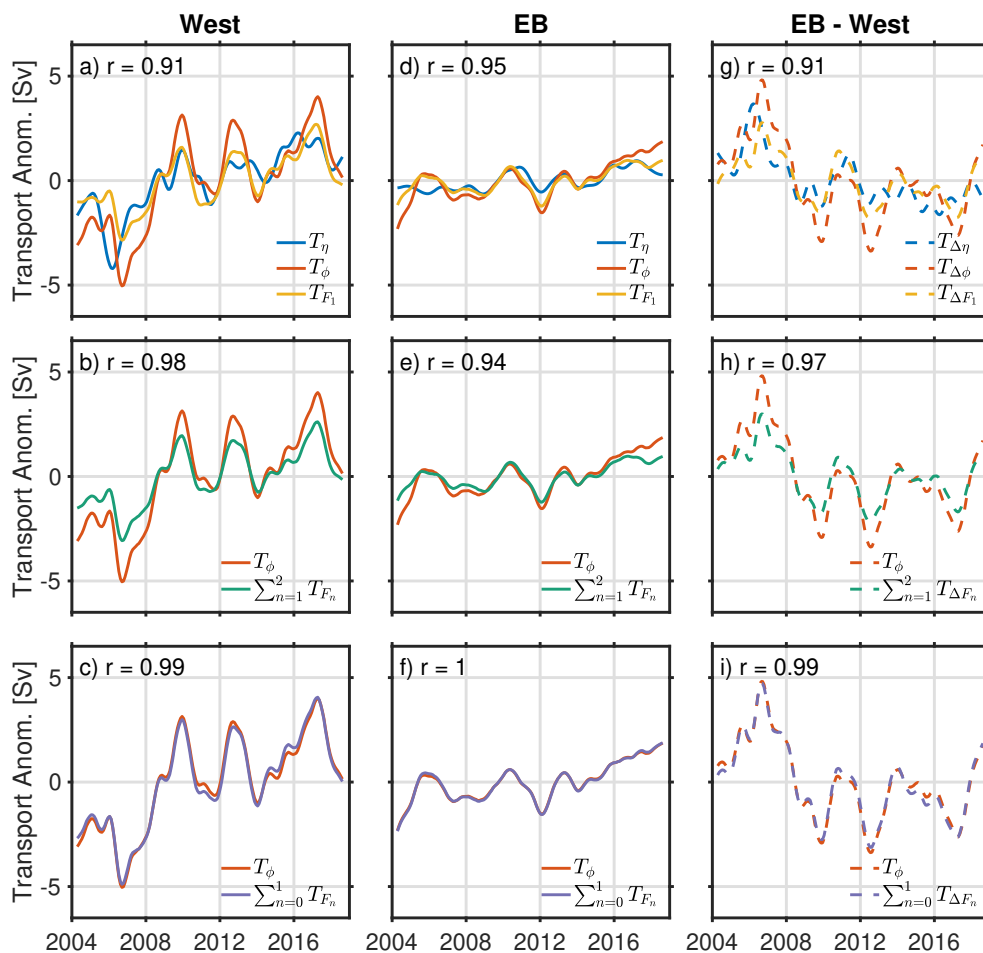
Figure 9. Transport anomalies estimated from dynamic height anomalies, T_ϕ (orange line), as per Eq. (13) at West (a,b,c), EB (d,e,f), and EB - West (g,h,i). Transport anomalies estimated from the reconstructed dynamic height anomaly, T_{F_n} as per Eq. (14), for mode 1 (yellow line; a,d,g), modes 1 and 2 (green line; b,e,h), and mode 0 and 1 (purple line; c,f,i) at West, EB, and EB – West respectively. Satellite-based transport, T_η (blue line), as per Eq. (15) is estimated in the (a) west (η at 27.875°N and 74.375°W), (d) east (η at 27.875°N and 13.125°W), and (g) east - west. Correlation between T_ϕ and T_F indicated in each plot. Units in Sv.
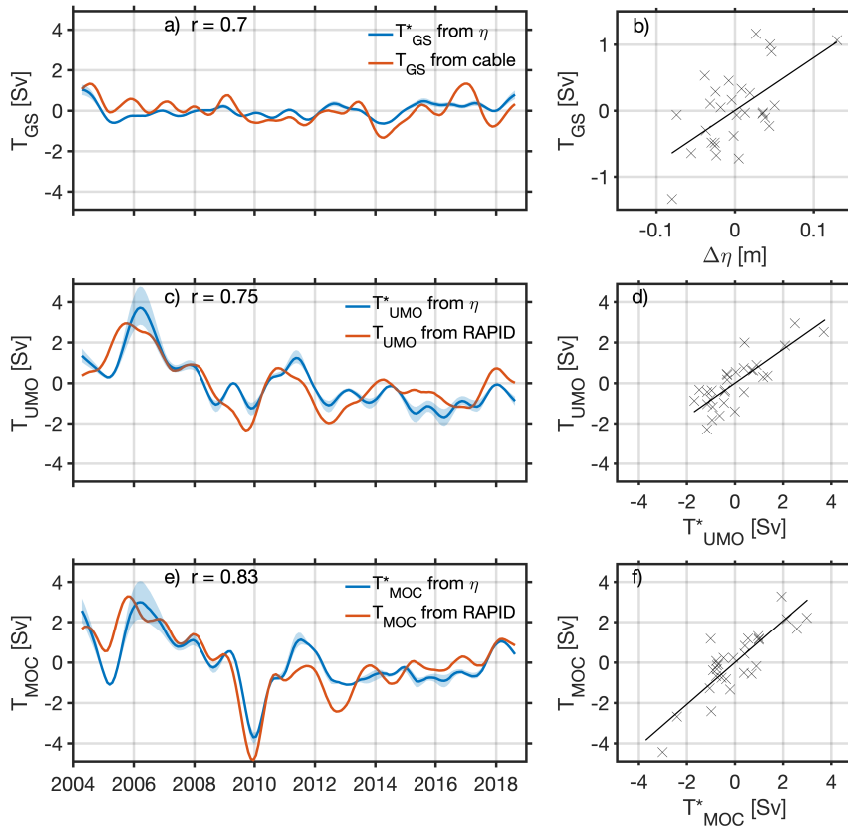
Figure 10. a) Time series of the Gulf Stream transport (T_{GS}) from submarine cables (orange line; (Baringer and Larsen, 2001)) and the satellite-derived T_{GS}^* estimates as per Eq. (18) (blue line). b) Scatterplot between the east (27.625°N and 77.125°W) - west (27.625°N and 80.125°W) SLA (η) and T_{GS} with the line of best fit linear regression - note y and x axis limits reduced to improved visibility of datapoints. c) RAPID upper mid-ocean transport (T_{UMO}; orange line) and the satellite-based T_{UMO}^* transport estimates as per Eq. (19) (blue line). d) Scatterplot between the T_{UMO}^* and T_{UMO} with the line of best fit linear regression. c) RAPID upper mid-ocean transport (T_{MOC}; orange line) and the satellite-based T_{MOC}^* transport estimates as per Eq. (19)(blue line). f) Scatterplot between the T_{MOC}^* and T_{MOC} with the line of best fit linear regression. Blue shading indicates uncertainty estimates using a Monte Carlo technique (a,c) as described in text, and blue shading in (e) is the sum of the confidence intervals from (a,c). In (b, d, f) data are subsampled once every 6 months. Units in Sv.
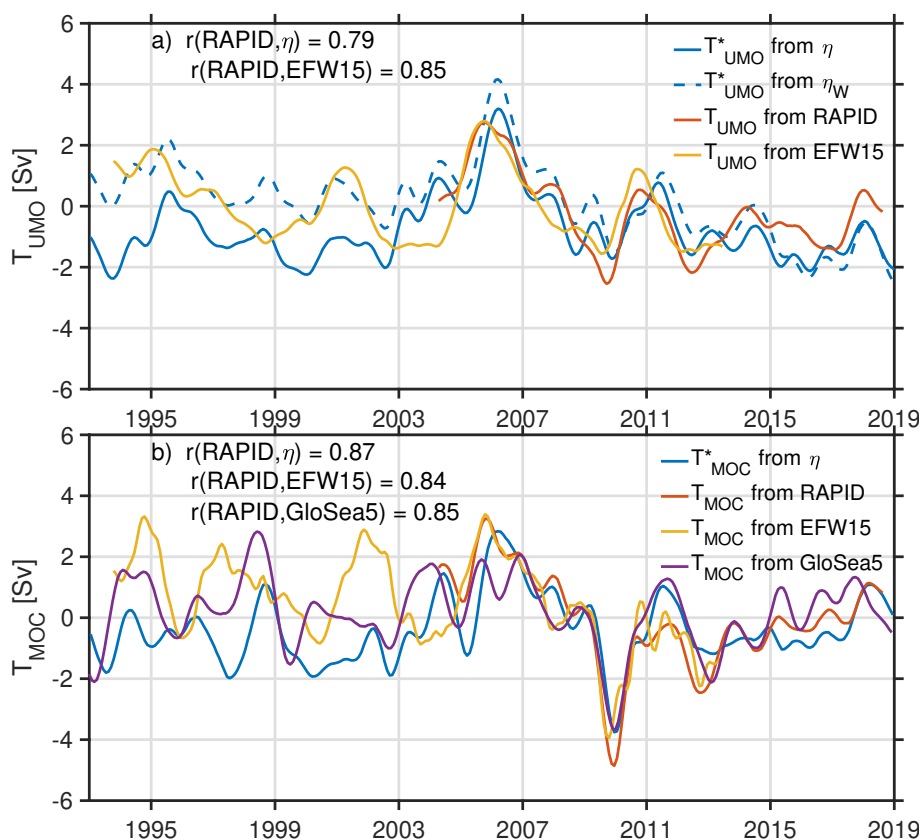
Figure 11. (a) The upper mid-ocean transport, T^*_{UMO}, from satellite (η) (blue line) as per Eq. (19), T^*_{UMO}, from η whilst the eastern component is held constant (blue dashed line), T_{UMO} from RAPID (orange line), and T_{UMO} from EFW15 (yellow line). (b) MOC transport, T^*_{MOC}, from η (blue line) as per Eq. (20), T_{MOC} from RAPID (orange line), EFW15 (yellow line), and GloSea5 (purple line). Correlations indicated in graphs are over the period of overlap between the RAPID and EFW15 time series, i.e. 2004 to 2013. Units in Sv.